Front. Struct. Civ. Eng. 2025, 19(4): 663–679
https://doi.org/10.1007/s11709-025-1182-7

RESEARCH ARTICLE

Effects of X-shaped Energy Dissipating Steel Dampers on the seismic response of high-speed railway track-bridge systems considering costs

Liqiang JIANG[a,b], Xiaozhi LIU[a*], Yingqi YAN[a], Lizhong JIANG[a,b], Yi HU[c]

[a] *School of Civil Engineering, Central South University, Changsha 410075, China*
[b] *National Engineering Laboratory for High-Speed Railway Construction, Changsha 410075, China*
[c] *School of Civil Engineering, Central South University of Forestry and Technology, Changsha 410004, China*
[*] *Corresponding author. E-mail: 234811029@csu.edu.cn*

ABSTRACT The high-speed railway track-bridge system (HSRTBS) is susceptible to damage under the effects of earthquakes, thus threatening the safety of running trains. To improve the seismic performance of HSRTBS and reduce damage to the system, a replaceable X-shaped Energy Dissipating Steel Damper (X-EDSD) is proposed, which contains the energy-dissipating component (EDC) to dissipate the earthquake energy. Cyclic tests were performed to obtain the hysteretic performance of the EDC and X-EDSD, and a test-validated numerical model was developed to conduct parametric analyses. The X-EDSD was simplified as a nonlinear spring element with hysteretic parameters and modeled into the numerical model of the HSRTBS for seismic dynamic analyses. The peak displacements of girder and rail decreased by approximately 48.1% and 47.7%, respectively. The peak deflections of the fasteners, cement asphalt mortar layer and sliding layer were reduced by 70.4%, 70.8%, and 86.1%, respectively. A comprehensive consideration of the system response control-economic cost ratio coefficient R_{pe} is proposed, and the optimal thickness of 14.94 mm is obtained by applying cubic term coefficient fitting according to 5 groups of steel plate thickness data for the specific case study in this paper. The method can be used for cost-informed X-EDSD-selection for seismic mitigation of HSRTBS.

KEYWORDS X-shaped energy dissipating steel damper, quasi-static test, high-speed railway track-bridge system, system response control-economic cost ratio coefficient

1 Introduction

China has a large proportion of bridges on high-speed railways because of its vast area and complex terrain [1]. Owing to the more active seismic activity in the West and the increasing number of high-speed railways heading to the West, bridges are at greater risk of seismic hazards [2–5]. Studies have shown that fixed bearing and track structures are vulnerable to damage [6]. Damage to the bearings can trigger overturning of the girder, and damage to the track structure can affect the safety of the train. Numerous studies have shown that vibration damping and isolation are the main and more recognized means of earthquake resistance.

Article history: Received Sep 25, 2024; Accepted Feb 15, 2025

In view of the good damping performance of bridge isolation technology, scholars in various countries have developed a variety of seismic isolation devices and conducted theoretical and experimental research on them [7,8]. Li et al. [7] proposed a curved steel tube damper which has better energy dissipation performance compared to steel tube dampers under the same conditions. Li et al. [8] proposed a simplified design method for nonlinear viscous damper parameters, which provided useful reference for long-span cable-stayed bridges. Wei et al. [9] utilized the Equal Strength Mild Steel Tunnel in a large span arch bridge, which can effectively control the displacement of the bridge. However, seismic isolation devices can cause large relative displacements, which threaten the track structure, rails, and even running trains.

To balance structural safety and track and rail deformation, an energy-dissipating damper is a better idea. More studies on X-shaped dampers have shown good energy dissipation. Karvanchi and Shekastehband [10] proposed X-type constraints, which were found to have very stable hysteretic responses and excellent energy dissipation. Liu et al. [11] proposed a stacked reinforced concrete shear wall with X-plate bracing, the addition of which had little effect on the stiffness degradation before yielding. Cao et al. [12] proposed a new type of buckling-restrained steel plate shear wall, and reported that the X-type restraining device can effectively inhibit the shear buckling of the infill steel plate and improve the seismic energy dissipation capacity of the shear wall. Ding and Zhao [13] proposed a pair of new X-shaped buckling restraint braces and reported that the samples were highly ductile and energy dissipative and eventually failed due to tensile fracture of the plate support. However, none of the above devices are used in high-speed railway bridges and are not easy to replace.

To summarize, this paper proposes a replaceable X-shaped Energy Dissipating Steel Damper (X-EDSD) on the basis of the replaceable energy dissipating damper device that has already been studied by the group [14,15]. The X-shaped steel plate has a good energy dissipation effect and the existing frame of the energy dissipation and vibration damping device can be quickly replaced [14,15]. A low cyclic test of the energy-dissipating component (EDC) in X-EDSD was conducted, and finite element models of X-EDSD for five different thicknesses of X-shaped steel plates were developed. The effect of X-EDSD imported into high-speed railway track-bridge system (HSRTBS) for controlling the response of the main components is analyzed. To select the optimal thickness X-shaped steel plate, a comprehensive consideration of the system response control-economic cost ratio (SRC-ECR) coefficient R_{pe} is proposed.

2 X-shaped Energy Dissipating Steel Damper

2.1 Configuration of X-shaped Energy Dissipating Steel Damper

The structural configuration of X-EDSD is shown in Fig. 1. The X-EDSD consists of an integral frame and 12 internal EDCs, with 6 EDCs on each side placed in parallel perpendicular to the inner and lateral steel tubes. The overall frame consists of an upper plate, a lower plate, a lateral steel tube and a middle steel tube. Bolts are used for connecting the EDC to the middle steel tube and lateral steel tubes of the overall frame. When an earthquake acts on the X-EDSD, the middle steel tube and lateral steel tubes undergo displacement misalignment, which tends to deform the EDC connected to it for energy dissipation. Since the upper plate and lower plate of X-EDSD are connected to the girder and pier, respectively, through pre-embedded bolt holes, X-EDSD can be easily replaced after damage, which is conducive to rapid post-earthquake repair of high-speed railway bridges.

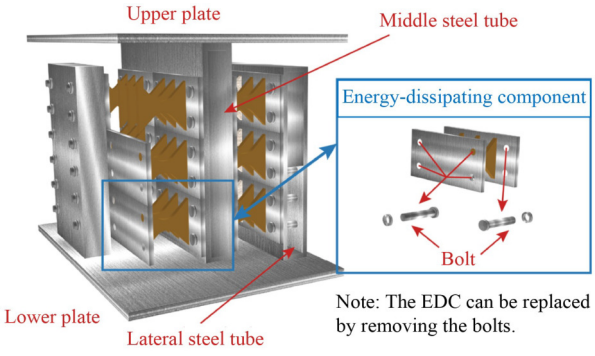

Fig. 1 X-EDSD structure construction diagram.

To study the seismic response analysis of the optimum thickness damper for HSRTBS under SRC-ECR analysis, the thickness of the X-shaped steel plate is varied. EDCs can be in the form of bending or shear energy dissipation dampers [16–18]. In this work, an X-shaped steel plate is used as the main component of the EDC, and a specific sample is shown in Fig. 2. The EDC consists of three X-shaped steel plates, which are perpendicular and welded to the two connection plates. The external forces acting on the EDC cause a displacement difference between the two plates in the longitudinal direction. The internal X-shaped steel plate undergoes bending and deformation for energy dissipation.

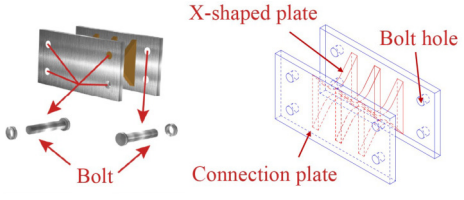

Fig. 2 EDC construction diagram.

The X-EDSD is a combination of 12 identical EDCs and is distributed on both sides of the middle steel tube, with three placed on each level. The X-EDSD is constructed of Q345 material and is shaped as a box with high stiffness, and the stiffness of the X-EDSD is fully sufficient. In addition, high-strength bolts were used to connect the X-EDSD to the EDCs, and the difference in deformation among all the EDCs is not significant and is considered to be consistent. In summary, the EDC is the main EDC in X-EDSD, and its hysteresis curve can reflect the hysteresis curve of X-EDSD.

2.2 Cyclic tests of energy-dissipating component

A low-cycle reciprocating test was conducted to obtain the hysteresis curve of the EDC. Figure 3 shows the dimensions and construction of the test specimen. The thickness of the X-shaped steel plate, the thickness and spacing of the connection plate, and the diameter of the screw connection holes are the most important parameters. Considering the symmetric arrangement of loading, the specimen force is more uniform. Therefore, the EDC is taken to be placed on the left and one on the right in the experimental setup, as shown in Fig. 3(d). The X-shaped steel plate is made of Q235 steel, and the rest are made of Q345 steel. As shown in Fig. 4, material properties tests were conducted on Q235 and Q345 steels. M-14 is Q235 steel and M-16 is Q345 steel. The material performance parameters are shown in Table 1.

The experimental specimens were subjected to a low cycle test via the MTS322 testing machine of Central South University. The specimen is placed as shown in Fig. 5(a). Figure 6 shows the loading method of test. The loading direction is vertical. Three sets of displacement amplitudes were classified on the basis of three different loading rates. The amplitudes were 0.25, 0.5, and 0.75 mm for a loading rate of 0.025 mm/s in the first stage. The amplitudes were taken as 2, 4, 6, and 8 mm for a loading rate of 0.1 mm/s in the second stage. The amplitudes were taken as 10, 15, 20, 25, and 30 mm for the third stage loading rate of 0.5 mm/s. Each level of amplitude was loaded twice.

The condition of the specimen after loading is shown in Fig. 5(b). When the loading rate and amplitude increase, the X-shaped steel plate bends seriously. In the final stage of loading, the X-shaped steel plate undergoes plastic deformation. Its damage clearly occurred at the welded joints, where cracking characterized the damage of the specimen.

The hysteresis curve can reflect the plastic deformation capacity of the structure and the energy dissipation ability. Figure 7(a) shows the hysteresis curve of the specimen. When the X-shaped steel plate inside the specimen bends and destructive fracture occurs at the weld seam, the load-carrying capacity decreases, and the strength decreases. The hysteresis curve of the surface specimen is more symmetric, which reflects that the specimen processing and testing process is more delicate and that the data are more reliable. The hysteresis curve is a relatively close image, indicating that the specimen has a good energy dissipation ability.

The skeleton curve of the test specimen can be obtained by connecting the peak force-displacement taken at each cycle, as shown in Fig. 7(b). An analysis of the skeleton curve, reveals that when the displacement is 1.99 mm, the specimen yields, and the yield force is 110.48 kN. When the displacement reaches 29.96 mm, the specimen is damaged and the ultimate bearing capacity is 275.61 kN.

The cumulative energy dissipated by the specimen during the test can be obtained by calculating the area

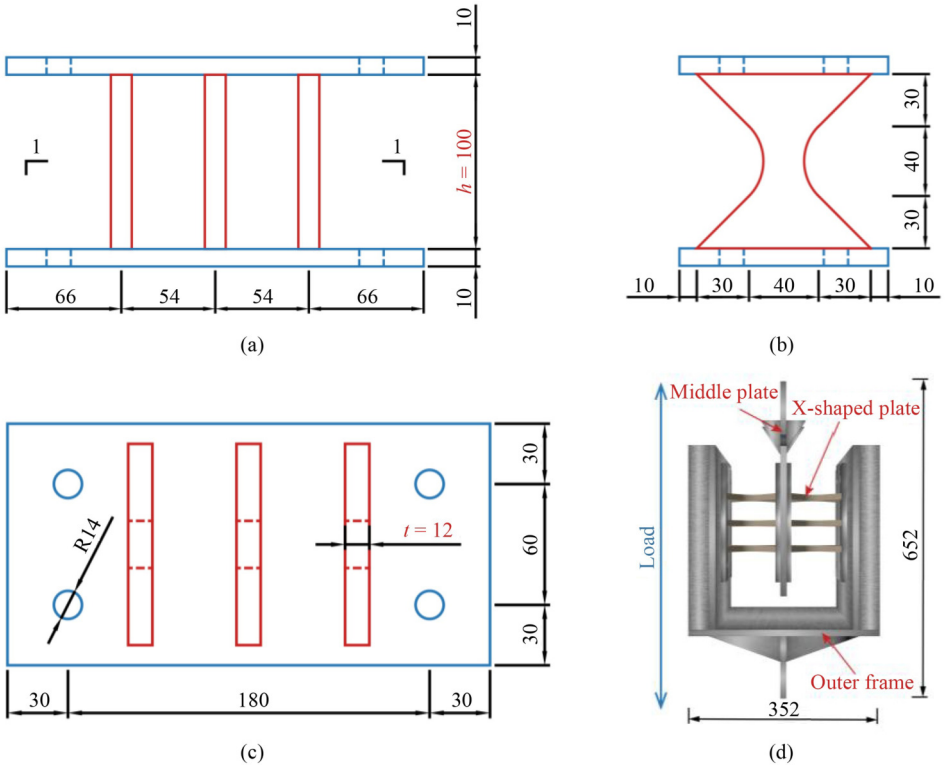

Fig. 3 Constructing style charts (unit: mm): (a) front view; (b) side view; (c) 1-1 cross-section; (d) configuration of specimen.

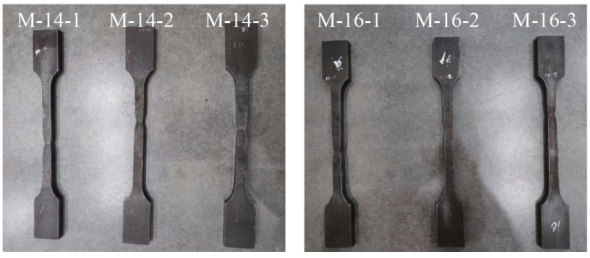

Fig. 4 Damage of steel material.

Table 1 Mechanical properties of steel material

Specimen	Elastic modulus, E (GPa)	Yield strength, σ_y (MPa)	Ultimate strength, σ_u (MPa)	Ultimate displacement, D (mm)
M-14-1	191.3	408.6	538.0	30.6
M-14-2	180.6	408.5	539.0	31.4
M-14-3	185.6	404.4	533.4	29.2
M-16-1	171.0	412.7	578.7	27.1
M-16-2	176.8	402.5	569.3	27.5
M-16-3	180.3	403.5	581.9	27.5

enclosed by the hysteresis curve, as illustrated in Fig. 8(a). Equivalent viscous damping ratios can be used to assess the effectiveness of the specimen in dissipating energy. The more effective the energy dissipation, the larger the corresponding coefficient. ζ_{eq} takes values ranging from 0 to 1. ζ_{eq} can be calculated via the following formula (JGJ101-96. 1996):

$$\zeta_{eq} = \frac{1}{2\Pi} \cdot \frac{S_{(CED+CFD)}}{S_{(OAE+OBE)}}. \quad (1)$$

The areas represented by $S_{(CED+CFD)}$ and $S_{(OAE+OBF)}$ are shown in Fig. 9. $S_{(CED+CFD)}$ is the area enclosed by the ellipse region and $S_{(OAE+OBF)}$ is the area enclosed by the triangle region.

Figure 8(b) shows the variation in ζ_{eq} with respect to the displacement of the specimen. The specimen clearly that the specimen exhibits elastic properties when the displacement is small. The displacement is large and the specimen experiences significant plastic deformation and exhibits nonlinear properties. This indicates an increase in the energy dissipation ability of the specimen. The data show that the maximum ζ_{eq} is 0.402. It is slightly larger than 0.39 which is the viscous damping ratio of the casting multi-plate damper suggested by Chen et al. [19], which indicates that the specimen in this paper has a greater plastic deformation capacity and energy dissipation performance.

3 Numerical analysis and hysteretic parameters of X-shaped energy dissipatingsteel dampers

3.1 Model validation of the energy-dissipating component

As shown in Fig. 10(a), the finite element model of the EDC in Abaqus is demonstrated along with the loading boundary conditions and loading method. The middle plate and outer frame are modeled as elastic-plastic materials. The modulus of elasticity of the material is 206 GPa and yield at 345 MPa. The middle X-shaped steel plate was modeled using Chaboche material [20]. The modulus of elasticity is 206 GPa and the material yields at 235 MPa. The welded and bolted joints are simulated by the tie constraint [21]. Therefore, the tie constraint is used for the constrained simulation of X-shaped steel plate, middle plate and outer frame.

Figure 10(b) shows the stress distribution of the specimen, and it shows that the EDC deformation characteristics are more in line with the test deformation for the bending X-shaped steel plate. The highest stresses occur near the outer frame and near the middle plate. The largest test bend is also here, and the surface finite element simulation is more consistent with the test.

The important mechanical parameters of the test and finite element analysis are given in Table 2. The yield displacement (D_y), yield force (F_y), initial stiffness (E_0), ultimate displacement (D_u), ultimate force (F_u) and

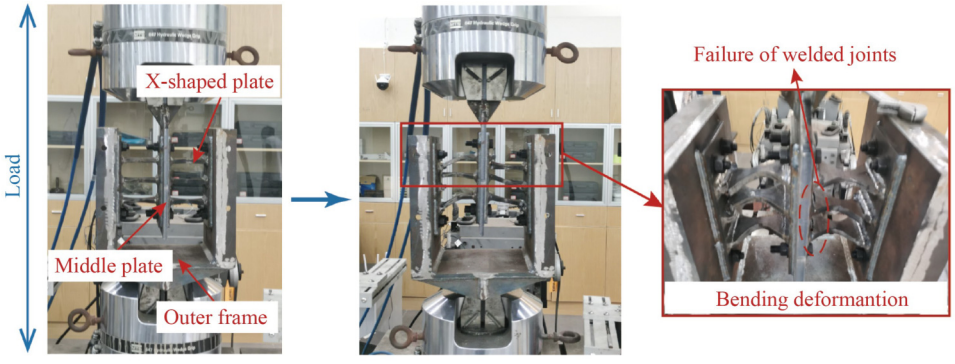

Fig. 5 Comparison before and after loading: (a) test setup; (b) failure pattern.

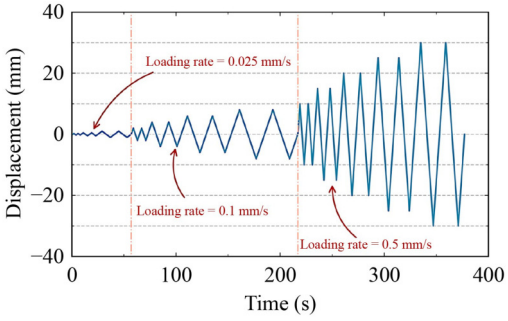

Fig. 6 Loading scheme.

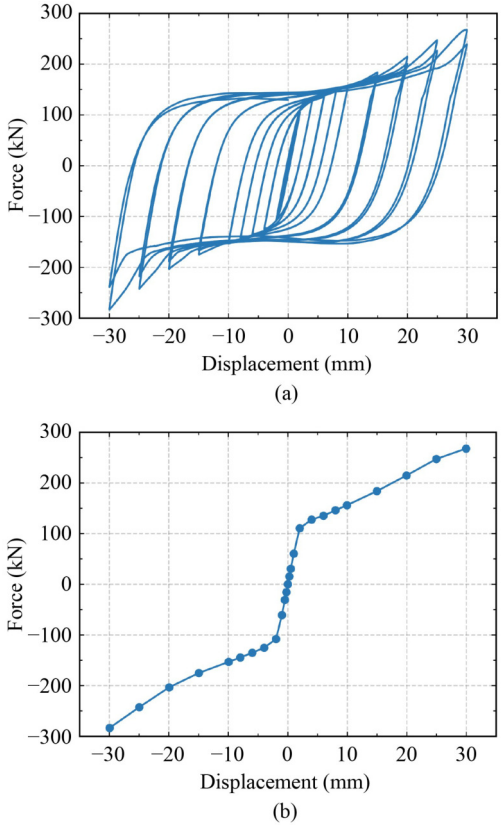

Fig. 7 Test hysteresis and skeleton curves: (a) the hysteresis curve; (b) the skeleton curve.

equivalent viscous damping ratio (ζ_{eq}) of the test and finite element model (FEM) are similar. Only the limit force (F_u) deviation is 24.43%. Because the more conservative processing of the test, welding and other processes are more delicate. The hysteresis curves of the final specimen versus the FEA specimens are shown in Fig. 11. Although the error in the limit force (F_u) reaches 24.43%, the equivalent viscous damping ratio (ζ_{eq}) differs by only 2.5% in terms of energy dissipation. Therefore, the finite element simulation of the EDC specimen is more reasonable and can be used for energy dissipation calculations.

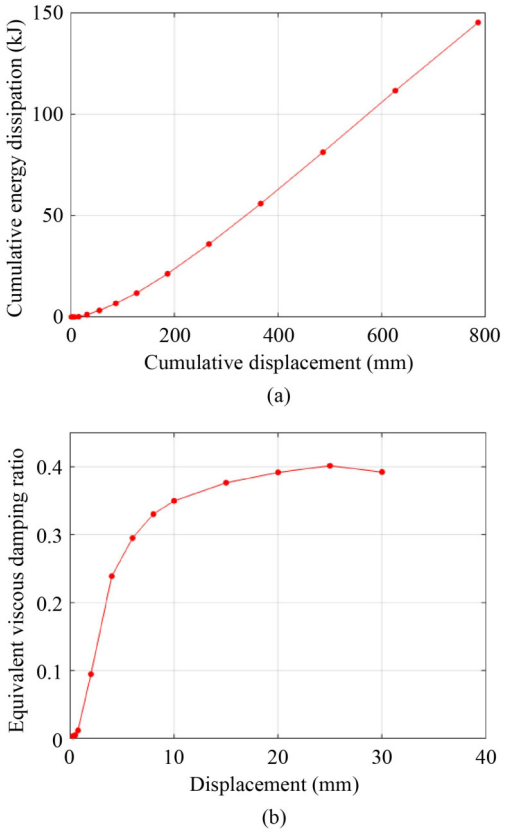

Fig. 8 Energy-dissipation performance: (a) cumulative energy dissipation; (b) equivalent viscous damping ratio.

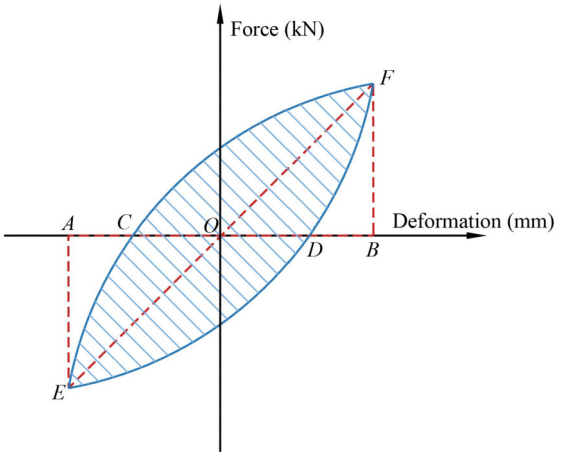

Fig. 9 ζ_{eq} calculation graph.

3.2 The finite element model of X-EDSDs

To select the most cost-effective X-EDSD, five X-EDSDs with different X-shaped steel plate thicknesses were established in this study. The thicknesses are 10, 12, 14, 16, and 18 mm. Their numbers are X-EDSD-10 (X10), X-EDSD-12 (X12), X-EDSD-14 (X14), X-EDSD-16 (X16), and X-EDSD-18 (X18).

All the components of X-EDSD use a 3D-stress 8-node

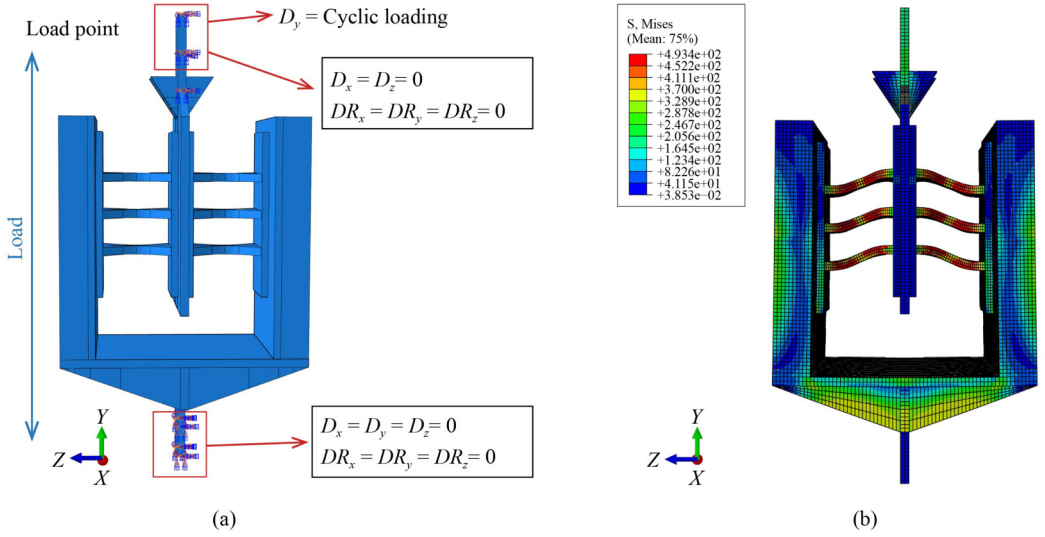

Fig. 10 EDC finite element model before and after damage: (a) boundary condition of the EDC; (b) stress distribution of the EDC.

Table 2 Comparison of key mechanical parameters

Conditions	D_y (mm)	F_y (kN)	E_0 (kN/mm)	D_u (mm)	F_u (kN)	ζ_{eq}
Test	3.68	192.89	52.42	29.96	275.61	0.40
FEA	3.55	180.76	50.92	29.99	221.03	0.41

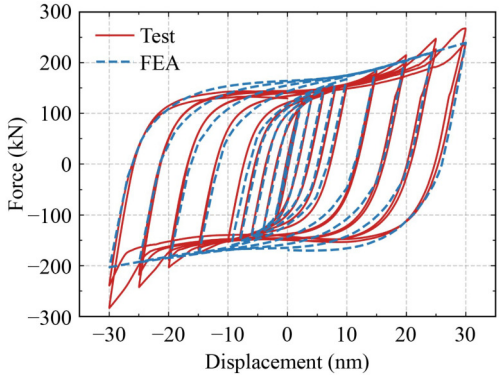

Fig. 11 Hysteresis curves of specimens with the finite element numerical model of X-EDSDs and the result.

nonlinear solid element (C3D8R) [15]. In addition, properties such as isotropy need to be considered. Therefore, the material model uses the Chaboche model [20] to simulate the properties of X-shaped steel plates in the EDC. Materials such as the X-EDSD outer frame and the connection to the EDC are modeled as ideal elastic-plastic materials. Its corresponding modulus of elasticity is 206 GPa, and it yields at 345 MPa. The tie constraint is adopted because the connection is more reliable and the actual EDC module is enough to connect to the X-EDSD. Therefore, tie constraint was used to simulate welded and bolted connections [21]. The FEM constraints and loading of X-EDSD are shown in Fig. 12(a). The final damage form and stress distribution are shown in Fig. 12(b). The damage pattern is similar to that of EDC, with higher stresses occurring at the edges of the X-shaped plate near the weld. This shows that X-EDSD has the same destruction mode as EDC does, validating the correctness of X-EDSD modeling.

The final hysteresis curves and skeleton curves of X-EDSDs are shown in Fig. 13. All the hysteresis curves are

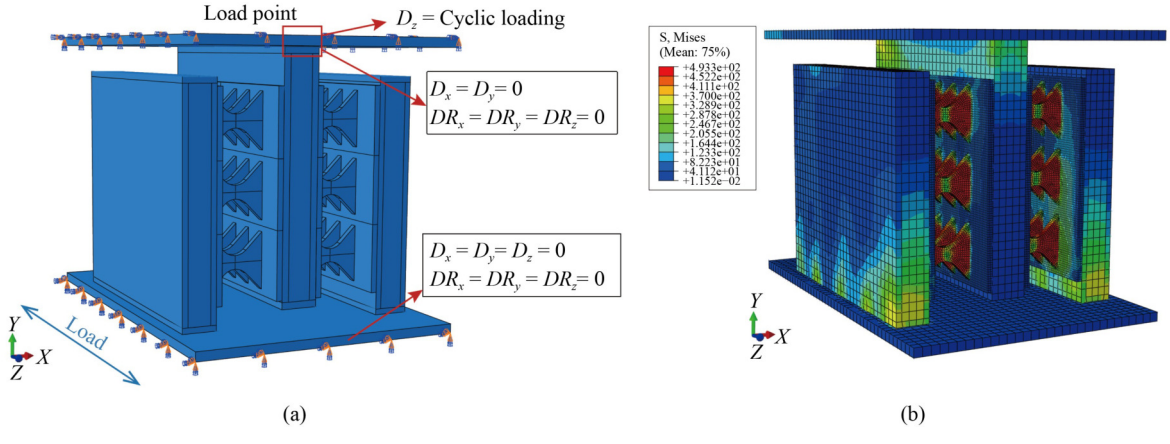

Fig. 12 Finite element model of X-EDSD: (a) boundary condition of the X-EDSD; (b) stress distribution of the X-EDSD.

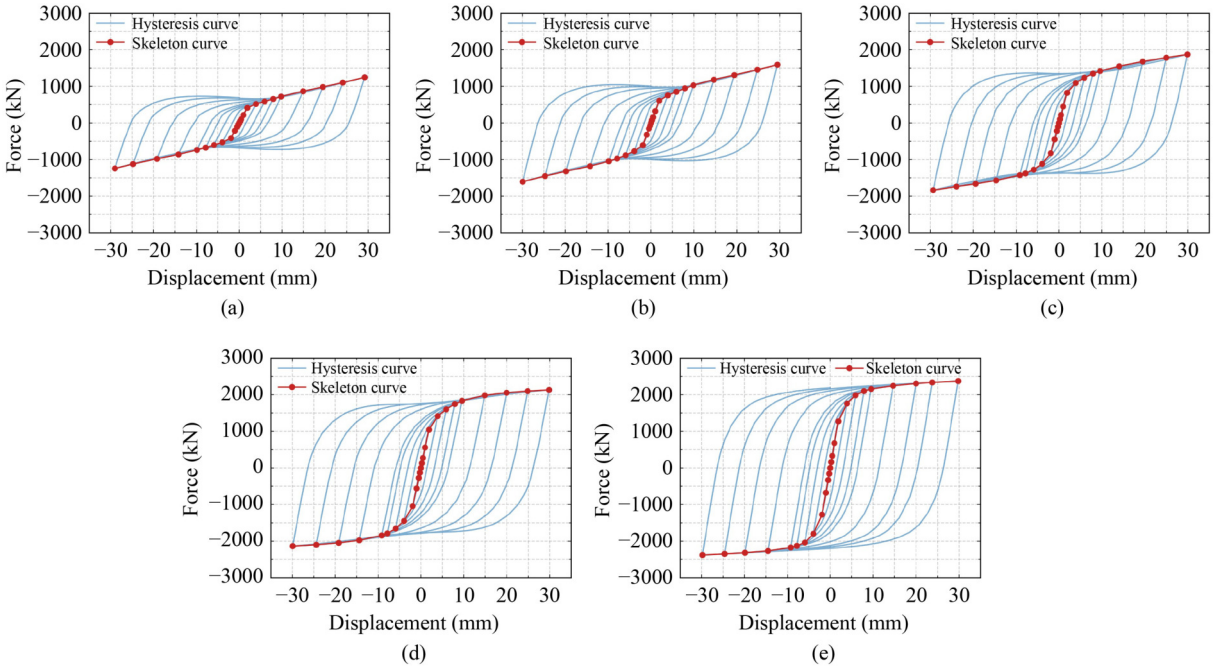

Fig. 13 Hysteresis and skeleton curves of X-EDSD: (a) X-EDSD-10; (b) X-EDSD-12; (c) X-EDSD-14; (d) X-EDSD-16; (e) X-EDSD-18.

closed graphs and relatively complete. As the thickness of the X-shaped plate increases, the corresponding hysteresis curve becomes fuller. This finding indicates that the greater the degree of energy dissipation, the greater the degree of plastic deformation.

The values of important parameters of X-EDSD are given in Table 3. The values of E_0, F_y, F_u, and ζ_{eq} increase approximately linearly. Because the X-shaped steel plate is elastic and its thickness changes linearly. The X-EDSD load carrying capacity and energy dissipation capacity increase with increasing X-shaped steel plate thickness. The viscous damping ratio ζ_{eq} of the tested specimen in the experiment is close to that of the X-EDSDs. This shows that X-EDSD composed of EDCs can fully utilize the energy dissipation ability of EDCs.

Table 3 Comparison of key mechanical parameters of X-EDSDs

Specimen	D_y (mm)	E_0 (kN/mm)	F_y (kN)	F_u (kN)	D_u (mm)	ζ_{eq}
X-EDSD-10	6.46	144.02	930.34	1244.78	29.23	0.35
X-EDSD-12	4.44	275.50	1223.23	1597.55	29.91	0.38
X-EDSD-14	3.59	424.32	1559.21	1854.64	29.91	0.42
X-EDSD-16	3.48	553.28	1925.42	2134.33	29.93	0.46
X-EDSD-18	3.26	677.31	2208.04	2375.27	29.83	0.50

4 A high-speed railway track-bridge system with X-shaped energy dissipating steel damper

4.1 Numerical model of the high-speed railway track-bridge system with X-shaped energy dissipating and steel dampers

The 3D model of a 5-span simply supported girder bridge containing X-EDSD is shown in Fig. 14. The bridge site type is Class I and the seismic design intensity is 8 degrees. The girder is a concrete box girder with a length of 32.5 m per span. The piers are round end shaped solid piers with a length of 14 m. Information about the dimensions of the girders and piers is shown in Fig. 15(a). In addition, there are subgrade sections on both sides, which are 140 m long. A 50 m long, 9 m wide, and 0.4 m thick friction plate was installed between the abutment and the T-shaped end thorns. The lower portion of the subgrade over the T-shaped end thorn edge is supported by a hydraulic bearing layer (HBL). The arrangement of bearings and X-EDSDs on the top of pier is shown in Fig. 15(b). The four types of bearings are fixed bearing (PZ-500-GD), horizontal moveable bearing (PZ-500-HX), longitudinal moveable bearing (PZ-500-ZX) and bidirectional moveable bearing (PZ-500-DX). The X-EDSD is arranged symmetrically with both sides of the bearing.

The track structure adopts a China Railway Track Structure II (CRTS-II) ballastless track system, which contains rails, track plates, base plates, fasteners, a cement asphalt (CA) mortar layer, a sliding layer, shear alveolars, and shear rebars. The distance between the base plate and the centerline of the girder is 2.5 m. Its material is C30 concrete. The dimensions are 2.95 m in width and 0.19 m in thickness. The width of the track plate is 2.55 m, the thickness is 0.2 m. Its material is C50 concrete. A CA mortar layer with a thickness of 0.03 m was installed between the track plate and the base plate. The rails adopt CHN60, and the fasteners adopt WJ-8. The shear alveolar

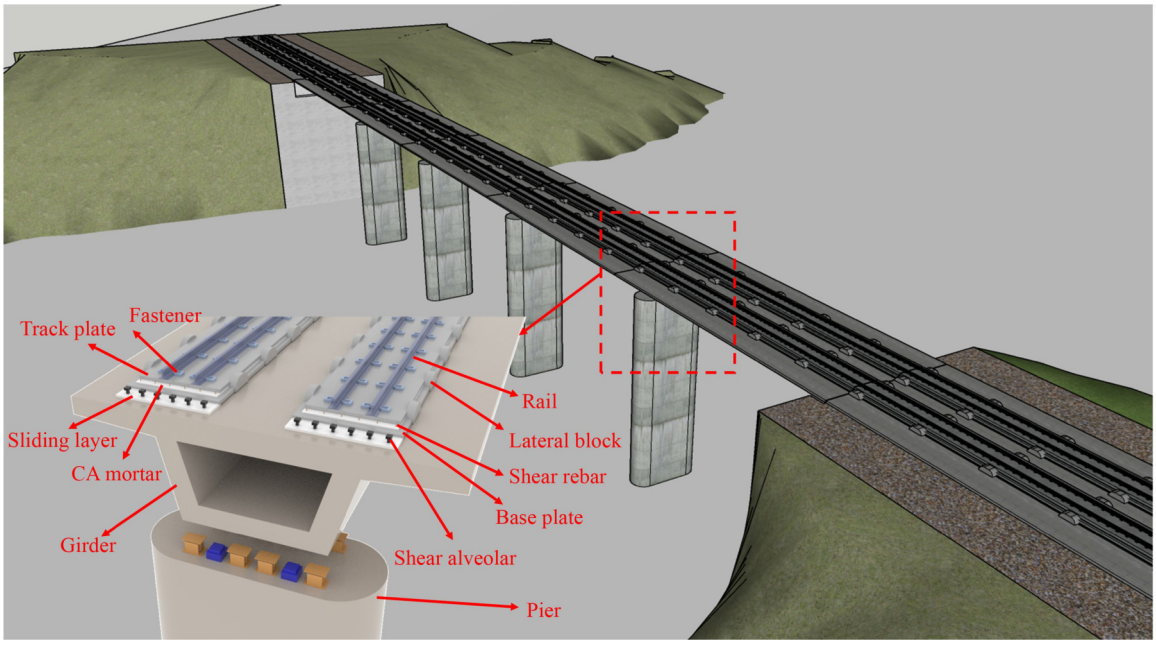

Fig. 14 3D modeling of the HSRTBS.

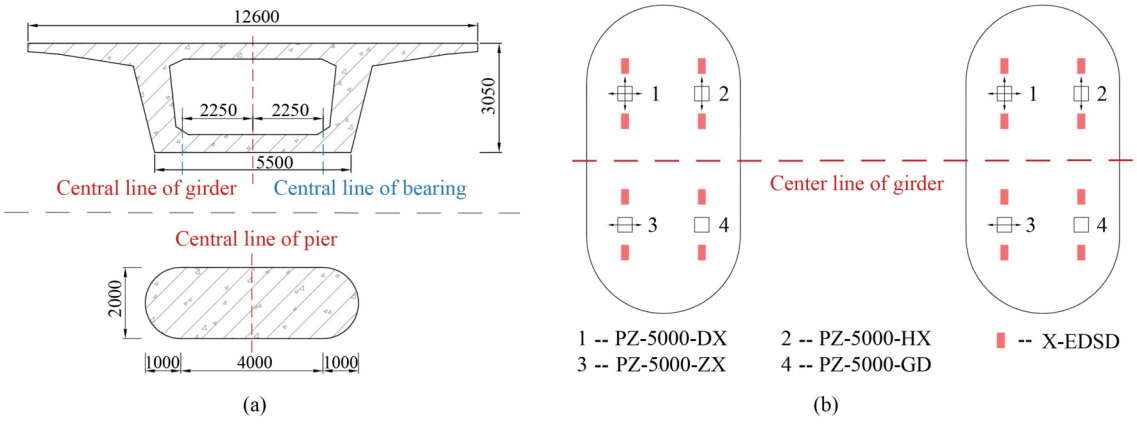

Fig. 15 Cross-sectional dimensions of the girder piers and bearing arrangement: (a) sections of the girder and pier; (b) layout of the bearing system.

is set in the upper part of the fixed bearing of each simply supported girder span to connect the girder with the base plate. Shear rebars are set at both ends of the girder joints on the bridge (including the abutment girder joints), and the function is to connect the two as a whole. The lateral blocks can limit the vertical displacement of the base plate and the track plate. Lateral blocks are arranged at 5.74 m intervals on simply supported girders and at 8 m intervals on friction plates. The top of the inverted T-shaped end thorn is cemented to the friction plate, and the base plate can transfer the longitudinal force of the base plate to the subgrade.

The HSRTBS containing the X-EDSD FEM is shown in Fig. 16. The probability of susceptibility to seismic lateral action can be reduced by simulating X-EDSD in parallel with zero-length elements [15] when the FEM is established via OpenSees. In this work, we consider only the transverse response reduction effect of X-EDSD on HSRTBS, since the transverse direction is the direction of weaker intensity [14]. In addition, the hysteresis curve of X-EDSD was simulated via the Pinching4 model [22]. Therefore, it is necessary to validate the ontology obtained from the Pinching4 model with the ontology obtained in Abaqus. As shown in Fig. 17, the X-EDSD hysteresis curve simulated by the chosen Pinching4 has less error than the hysteresis curve obtained in Abaqus. Thus, it is reasonable to use the Pinching4 model to simulate X-EDSD in HSRTBS.

Figure 16 illustrates the FEM, which results in less damage to the girder, friction plate, HBL, rails, track plate and base plate under seismic action [23]. They are simulated by elastic beam element, and the element has a length of 0.65 m [24]. The corresponding material properties [14] are shown in Table 4. Fixed bearings,

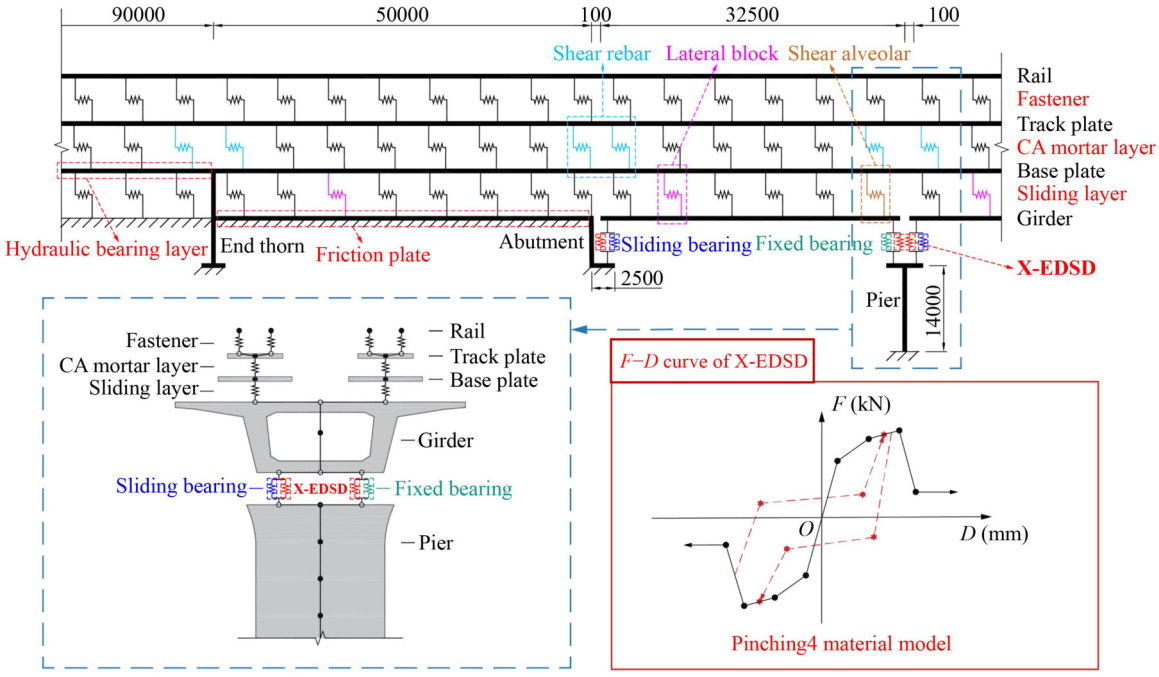

Fig. 16 Finite element model of HSRTBS with X-EDSD.

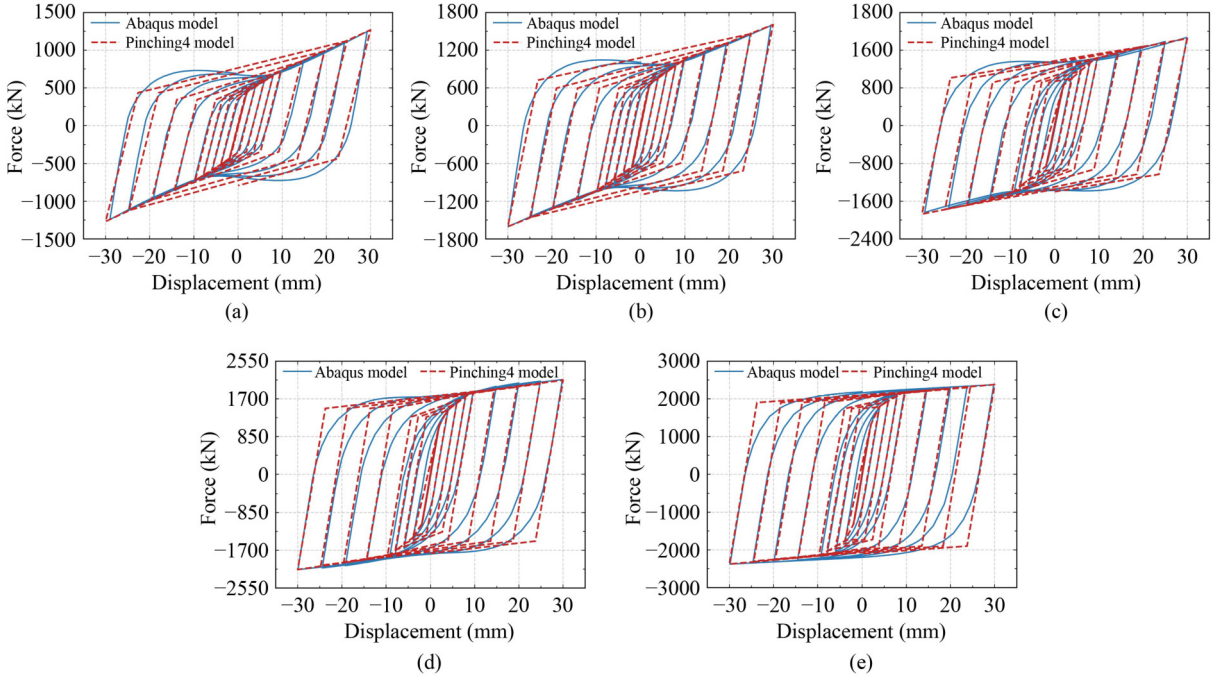

Fig. 17 Hysteresis curves of X-EDSD in HSRTBS: (a) X-EDSD-10; (b) X-EDSD-12; (c) X-EDSD-14; (d) X-EDSD-16; (e) X-EDSD-18.

Table 4 Material properties of the elastic beam-column element

Component	Material	Elastic modulus (MPa)	Poisson's ratio	Density (kg/m^3)
Girder	concrete (C50)	3.45×10^4	0.2	2500
Friction plate	concrete (C50)	3.45×10^4	0.2	2500
HBL	hydraulic material	1.80×10^3	0.2	2500
Rail	steel (Q235)	2.06×10^5	0.3	7250
Track plate	concrete (C55)	3.55×10^4	0.2	2500
Base plate	concrete (C30)	3.00×10^4	0.2	2500

sliding bearings, fasteners, CA mortar layers, sliding layers, shear alveolars and shear alveolars are simulated by zero-length spring elements [23]. The spacing of the zero-length spring elements is 0.65 m and the force-displacement curves are given in Table 5. The specific parameter values [25–30] are shown in Table 5. The four types of bearings are established in the Finite element model. The mechanical parameters of them are shown in the Table 5. Through changing the mechanical parameters of them to control the characteristic of them. In addition, the dimensional effect of the interlayer connection is ignored when modeling because the dimensions of the interlayer connection in the vertical direction are much smaller than the dimensions of the component [23,31–33].

Nonlinear beam elements with fiber cross sections can better model piers [34–36]. The peak strain of the cover concrete is 0.2% and the ultimate strain is 0.4%. The simulations were performed via the Concrete01 model [37]. The core concrete is simulated by the Concrete04 model [22], which considers the hoop constraints of the piers. The longitudinal reinforcement of the pier is HRB400. It yields at 400 MPa, and the modulus of elasticity is 206 GPa. The abutments and piers are connected to the ground with fixed constraints [38]. Considering that the material used was different from the prototype piers, the hysteresis curves for the piers were verified. Shao et al. [39] obtained hysteresis curves for piers via low cyclic tests. The specimen parameters are listed in Table 6, and the hysteresis curves are compared in Fig. 18. Considering the error of the material and the error of measurement, the experimental results and the FEA results are considered to be similar, and this model of the pier can be used for the finite element calculation and analysis of HSRTBS.

Table 5 Properties of the zero-length element

Component	Horizontal direction				Vertical direction	
	F–D curve	D_t (mm)	F_t (kN)	D_l (mm)	F_l (kN)	F–D curve	K_v (kN/mm)
Fixed bearing	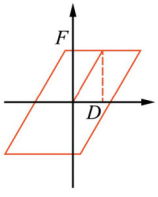	2	1000	2	1000	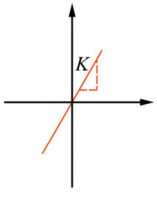	1.0×10^4
Moveable bearing		2	100	2	100		1.0×10^4
Fastener		2	24	2	9		24
CA mortar layer		0.5	42	0.5	42		2.0×10^3
Sliding layer		0.5	14	0.5	14		–
Shear rebar		0.075	23	0.075	23		2.0×10^3
Shear alveolar		0.12	1465	0.12	1465		2.0×10^3
Lateral block		2	453	0	0		2.0×10^3

Notes: D_t and F_t are the deformation and force of the component in the transverse direction, respectively; D_l and F_l are in the longitudinal direction.

Table 6 Parameters of piers

Number	H (m)	$\lambda = H / T$	$N / (f_c A_g)$ (%)	ρ_s (%)	ρ_v (%)
SOL-6	2.0	5.3	5	0.75	0.15
SOL-9	2.0	5.3	10	0.15	0.30
SOL-11	3.0	8.0	10	0.75	0.45

Notes: H is the height of the pier, T is the width of the pier, λ is the aspect ratio of the pier, N is the axial force , f_c is the design value of axial compressive strength of concrete , A_g is the cross-sectional area of the pier, $N / (f_c A_g)$ is the axial load ratio, ρ_s is the longitudinal reinforcement ratio, and ρ_v is the Stirrup ratio.

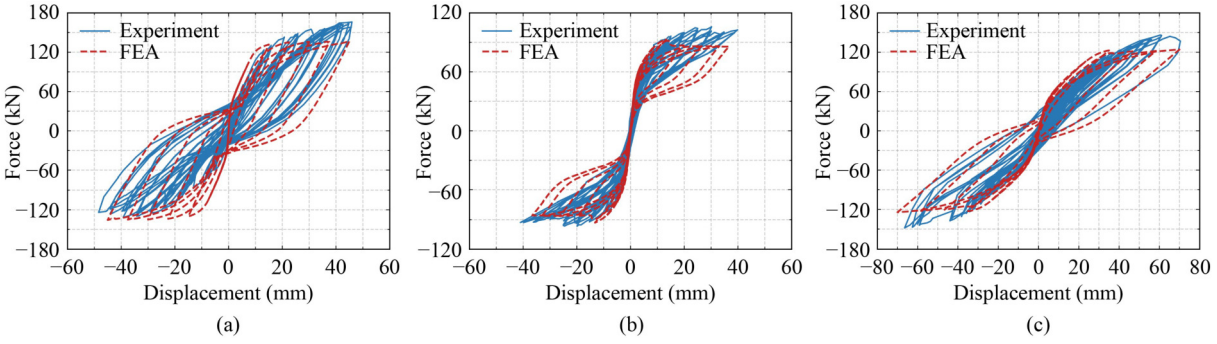

Fig. 18 Comparison of pier hysteresis curves: (a) SOL-6; (b) SOL-9; (c) SOL-11.

4.2 Model verification

Jiang et al. [23] conducted a shaking table test on the HSRTBS model and validated that the HSRTBS model is reasonable [31]. The experimental and finite element results revealed that the difference in peak acceleration at the top of the pier was 8.3%, the difference in deformation values of the CA mortar layer was 17%, and for the fixed bearing it was 11% [23,31]. Considering the errors in the experiments and deviations in the material properties, the HSRTBS model is reasonable.

4.3 Selected ground motion records

The bridge used for the model is located on a Class I site with a seismic intensity of 8 degrees. The corresponding site design spectra were selected in accordance with the Code for Seismic Design of Railway Engineering of China [40]. Forty earthquake records were selected from the response spectra to the Pacific Earthquake Engineering Research Center (PEER). Considering that the transverse direction of the HSRTBS is the weaker direction [24,41], the selected earthquake records act in the transverse direction of the HSRTBS and record the time-history responses of the key components. Twenty-one records are near-fault non-pulsed records (NNs) and the remaining 19 are near-fault pulse-like records (NPs). As shown in Fig. 19, the peak ground acceleration of the selected earthquake records is between 0.39g and 1.03g and the magnitude is between M_w6.90 and M_w7.10.

5 Evaluation of the seismic responses of high-speed railway track-bridge system with X-shaped energy dissipating steel dampers

5.1 Effect of X-shaped energy dissipating steel dampers

As shown in Table 7, the mode of HSRTBSs changed slightly when install the X-EDSDs. Moreover, when the thickness of X-EDSD increases to 12, the mode frequency remains basically unchanged. Therefore, the thickness of X-EDSD has little effect on the mode.

To better evaluate the specific damage states of the key components, the indexes for different damage states quantified by the existing research results are introduced [42,43]. As shown in Table 8, the piers were determined via the drift ratio of the pier top, and the remaining components were determined via the deformation values in mm. There are 4 levels of damage states. They are slight damage, moderate damage, severe damage and complete damage.

Figure 20 shows the displacement values of the girder. In the figures, BTS means the Bridge-Track system with no X-EDSDs, and the BTS-X10 means the Bridge-Track system with the X-EDSD-10. After setting the X-EDSD, the X-EDSD reduction effects of all five groups are similar and great. The thicker the corresponding X-shaped steel plate is, the greater the reduction. X-shaped steel plates with a thickness of 18 mm reduced the maximum displacement from 120.8 to 62.7 mm, a reduction of 48.1%. A similar phenomenon was found with the fixed bearing, as shown in Fig. 21. All the fixed bearing deformations were significantly reduced. When the X-EDSD with 10 mm steel plate thickness, the damage index of the fixed bearing on the Pier 3 was still in a severe damage state, and the effect was quite different from those of the remaining 4 types. X-EDSD with 16 and 18 mm steel plate thickness reduces all bearing responses to slight damage with the best results, effectively reducing the risk of the girder tipping over and falling onto the girder. However, X-EDSD amplifies the pier displacement response, as shown in Fig. 22. Because the presence of X-EDSD increases the stiffness of the system composed of piers and bearings [14,15], which causes the piers to be subjected to greater seismic forces. The five thicknesses of the X-shaped steel plates are close to each other in terms of increasing the response of the

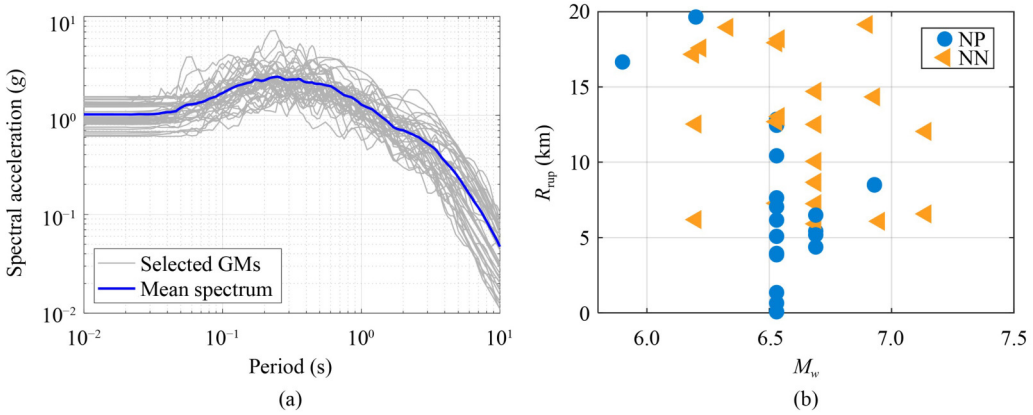

Fig. 19 Information on selected ground motion records: (a) selected seismic wave response spectra; (b) distribution of ground motion records.

Table 7 The mode of HSRTBSs

Condition	Mode frequency (Hz)									
	1	2	3	4	5	6	7	8	9	10
HSRTBS	21.13	22.84	25.52	26.36	32.67	35.63	47.70	50.15	59.72	66.24
HSRTBS-X10	24.01	25.52	25.90	29.31	36.70	38.90	47.70	54.64	65.74	66.24
HSRTBS-X12	24.40	25.52	26.32	29.76	37.39	39.57	47.70	55.42	66.24	66.93
HSRTBS-X14	24.40	25.52	26.32	29.76	37.39	39.57	47.70	55.42	66.24	66.93
HSRTBS-X16	24.40	25.52	26.32	29.76	37.39	39.57	47.70	55.42	66.24	66.93
HSRTBS-X18	24.40	25.52	26.32	29.76	37.39	39.57	47.70	55.42	66.24	66.93

Table 8 Damage states of key components (mm) [42,43]

Component	Boundary value of damage state (deformation)			
	Slight damage	Moderate damage	Severe damage	Complete damage
CA mortar layer	0.5	1	1.5	2
Sliding layer	0.5	1	1.5	2
Fixed bearing	2	4	6	8
Fastener	2	3	4	5
Pier (drift ratio of pier top)	0.13%	0.34%	0.95%	2.05%

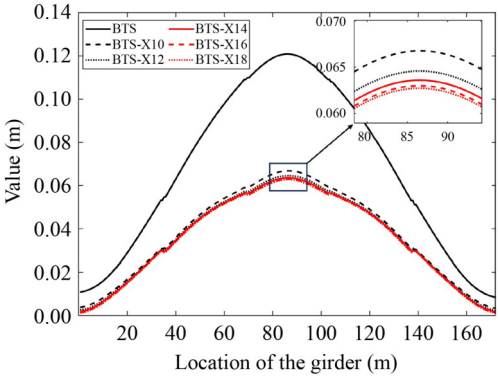

Fig. 20 Girder displacement along the bridge direction.

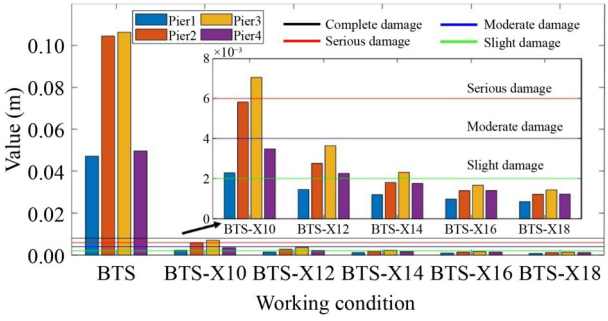

Fig. 21 Deformation of fixed bearings.

pier, which gradually tends to stabilize. Considering that the side piers are only slight damaged, the middle pier top displacement ratio of 0.392% is just above the limit for moderate damage (0.34%) and far from the limit for severe damage (0.95%). Therefore, the superstructure risk

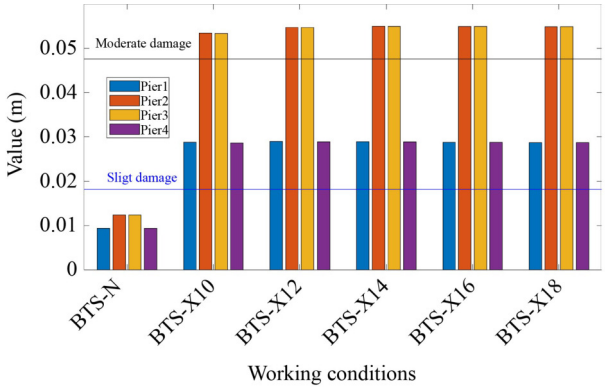

Fig. 22 Displacement of the top of the piers.

can be transferred to piers by installing X-EDSD, and the piers are in safe conditions.

Figures 23–26 show the peak response of the components of the track structure. The X-EDSD effectively controls the peak response of the track structure. Thicker X-plates correspond to a more pronounced decrease in response. The specimen with the 18 mm X-shaped steel plate that exhibits the best performance. The following analysis takes it as an example. As shown in Fig. 23, the maximum displacement of the rail was reduced from 120.8 to 63.2 mm, a reduction of 47.7%. The fasteners and CA mortar layers were slightly damaged. Fig. 24 shows that the maximum deformation of the fastener decreased from 0.71 to 0.21 mm, a decrease of 70.4%. Figure 25 shows that the maximum deformation of the CA mortar layer was reduced from 0.48 to 0.14 mm, a reduction of 70.8%. As shown in Fig. 26, the damage index of sliding layer was reduced most significantly. The maximum deformation of the sliding layer was reduced by 86.1%, which decreases from the 7.64 mm complete damage state to the 1.06 mm moderate damage state.

5.2 Optimal selection of X-shaped energy dissipating steel damper for the high-speed railway track-bridge system

Since the effect of X-EDSD on the component of the HSRTBS are different, the evaluation of the degree of damage to the HSRTBS should favor the reduction effect of the whole system. When analyzing a single

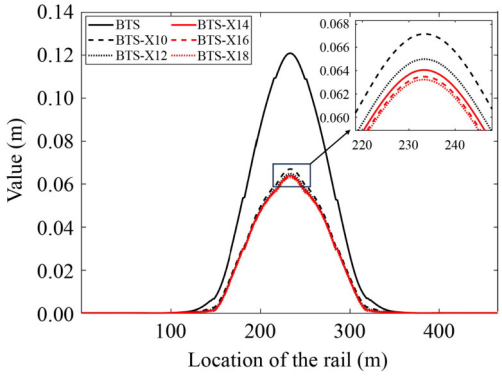

Fig. 23 Rail displacement along the bridge direction.

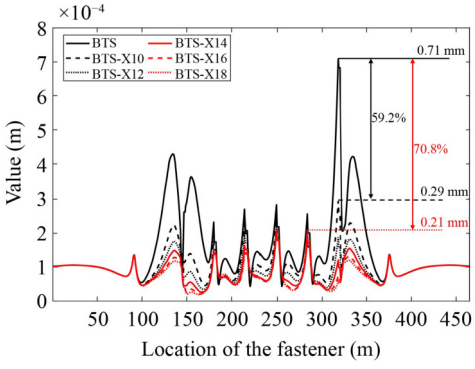

Fig. 24 Deformation of fasteners along the bridge.

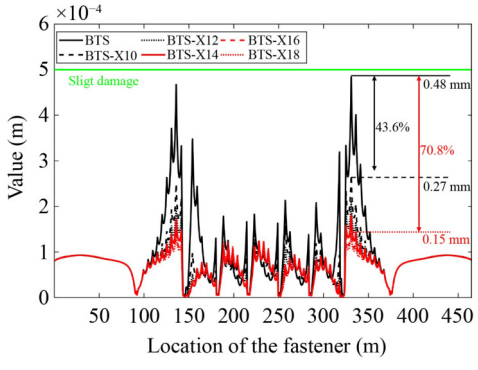

Fig. 25 Deformation of the CA mortar layer along the bridge.

component, the average reduction of all the same components should also be considered. Therefore, this study considers the average reduction of a component which is not just the peak response effect. The thicker the X-shaped steel plate is, the greater the response reduction. However, the thicker the X-shaped steel plate is, the greater the cost. Therefore, a response economic coefficient R_{pe} is proposed. The R_{pe} synthesizes the effect of X-EDSD on the system response control with the cost of X-EDSD:

$$R_{pe} = R_s C, \tag{2}$$

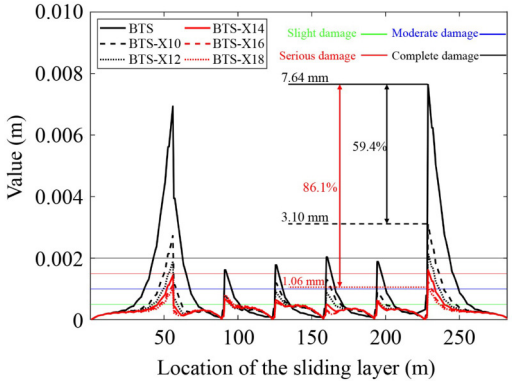

Fig. 26 Sliding layer deformation along the bridge.

where R_s is the system response control ratio, and C is the cost ratio of X-EDSD.

R_s is the control value of X-EDSD for the integrated response of important HSRTBS components, which is considered to evaluate the response control effect of X-EDSD for the whole system. It is calculated in the following way:

$$R_s = \sum_{i=1}^{7} IF_i R_{si}, \tag{3}$$

$$R_{si} = \frac{1}{n}\sum_{j=1}^{n} \frac{D_{Xj}}{D_{Nj}}, \tag{4}$$

where i is the number of component types considered, IF_i is the importance factor of the component, and R_{si} is the response reduction ratio of the specific component in the HSRTBS [14]. n is the total number of the corresponding quantities in HSRTBS for each specific component, j is the jth component in the same type of the specific component, D_X is the response value of the component after the addition of X-EDSD, and D_N is the response value of the component without the X-EDSD set.

The importance coefficient IF_i is taken with reference to the existing research [44], and finally the weighted index percentage is used to derive the importance coefficient IF_i of the corresponding component [45]. The importance factor is 9 because the deformation of the bearing is directly related to whether the girder falls. Greater deformation of fasteners leads to greater rail displacement, thus affecting the running speed and safety, so the importance factor is 5. Previous studies [46] have shown that both the sliding layer and CA mortar layer have less of an impact on the HSRTBS. The importance factor for the track plate and base plate takes a value of 1 [44], so the importance factor for the sliding layer and the CA mortar layer also takes a value of 1. The final values of the importance factor and IF_i for the considered components are shown in Table 9.

In view of the impact of various currencies and price

Table 9 The importance factor and IF_i of each component

Component	Attribute evaluation	IF_i	Importance factor	Source
Rail	extremely important	0.243	9	[44]
Bearing	extremely important	0.243	9	This paper
Girder	very important	0.190	7	[44]
Fastener	important	0.135	5	This paper
Pier	important	0.135	5	[44]
Sliding layer	less important	0.027	1	This paper
CA mortar layer	less important	0.027	1	This paper

differences between regions, the X-EDSD price ratios consisting of different X-shaped steel plate thicknesses are proposed as the cost factor. The previous analytical results indicate that the difference in response control is greater for the 10 mm thick X-shaped steel plate than for the 18 mm thick X-shaped steel plate. Therefore, it can be assumed that the optimum thickness of the X-shaped steel plate is greater than 10 mm. In the existing 5 groups of conditions, the price of 10 mm thick X-shaped steel plate is selected as the benchmark, and the price of the remaining X-shaped steel plate and its ratio are the corresponding cost ratios, which are calculated via the following formula:

$$C = \frac{Cost - t}{Cost - 10}, \tag{5}$$

where $Cost{-}t$ is the total cost of X-EDSD with thickness t.

At the time of test preparation, the total cost of X-EDSD fabrication consisted of material costs as well as processing costs. The material cost is the price of the steel required for the X-EDSD, which can be obtained by multiplying the steel price by the quality of the corresponding X-EDSD. The price of steel can be obtained through the steel market, where the average price of steel in China over the past few years has been 4500 RMB/t. Before the test, we need to cut the X-shaped steel plate and other processing processes, and the price of such processes is not related to the thickness of the steel plate; rather, it is a fixed value. The cost required for test preparation and processing, is approximately \$1568.69. The final detailed cost of X-EDSDs is obtained as shown in Table 10.

Figure 27(a) shows the control value R_s for different thicknesses of X-EDSD for the overall response of the HSRTBS component. As the thickness of the X-shaped steel plate increases, the value of R_s decreases. The thicker X-shaped steel plate is more effective in controlling the overall response of the HSRTBS components. However, the optimal solution of X-EDSD cannot be selected by using the HSRTBS component response control effect alone. The effect of its cost also needs to be considered.

Figure 27(b) shows the values of the SRC-ECR coefficients R_{pe} for different thicknesses of X-EDSDs. Among the five X-EDSDs, the 16 mm X-shaped plate thickness yields the best results, followed by 14 mm. They can be considered to have the same SRC-ECR control effect. To obtain the optimal thickness, a third-degree polynomial was fitted for the five data sets and the resulting curve equations are shown in Fig. 27(b). The calculations yielded an optimal thickness is 14.94 mm, corresponding to an R_{pe} value of 0.9455. Therefore, in the HSRTBS model used in this study, the SRC-ECR control is considered to be best when the X-EDSD thickness is 14.94 mm. Considering the actual machining progress, it

Table 10 The cost coefficients of X-EDSDs

Cost content	DX-10	DX-12	DX-14	DX-16	DX-18
Volume (cm^3)	37006.1	37726.1	38446.1	39166.1	39886.1
Quality (t)	290.4979	296.1499	301.8019	307.4539	313.1059
Material cost	1307.24	1332.67	1358.11	1383.54	1408.98
Processing cost	1568.69	1568.69	1568.69	1568.69	1568.69
Total cost	2875.93	2901.36	2926.80	2952.23	2977.67
Cost coefficient	1.000	1.009	1.018	1.027	1.035

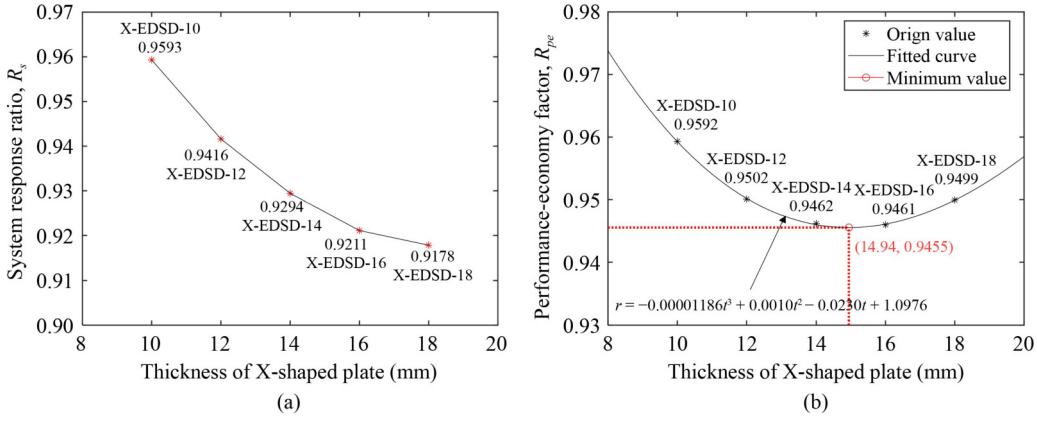

Fig. 27 Comprehensive evaluation of response control on the basis of cost ratio: (a) system response ratio; (b) performance-economy factor.

is difficult to achieve such high values. A value of 15 mm is recommended.

6 Conclusions and discussion

This paper presents an easily replaceable X-EDSD device for controlling the response of HRSTBS components under earthquake. To obtain the hysteresis curve of X-EDSD as well as the damage form, a low cycle test was carried out on a specimen consisting of EDC, which is the main EDC. Considering the large influence of different thicknesses of X-shaped steel plates on the effect of X-EDSD, five finite element models of X-EDSD with different thicknesses of X-shaped steel plates were established. A nonlinear time-course analysis was performed after introducing it into HSRTBS. To derive the X-EDSD for the optimal X-shaped steel plate thickness, the SRC-ECR evaluation method is proposed, and the conclusions are drawn as follows.

1) The hysteresis curves from the EDC tests of the EDCs in X-EDSD are more complete closed graphs with larger equivalent viscous damping rates. The specimen can be considered to have a great capacity to dissipate seismic energy. A finite element simulation of the EDC was carried out via the Chaboche material model. It shows that the hysteresis curves of the finite element model were basically in good agreement with the skeleton curves and those obtained from the EDC tests. Therefore, this finite element simulation is valid.

2) The results of the finite element hysteresis curves established for five different thicknesses of X-EDSD show that the thicker the X-shaped steel plate is, the greater the load carrying capacity and initial stiffness corresponding to X-EDSD. The viscous damping ratio changes more stably with increasing X-shaped steel plate thickness, and the energy consumption performance steadily improves. X-EDSD can effectively utilize the energy consumption performance of the EDC.

3) HSRTBS response control works best for the X-EDSD with an 18 mm thickness X-shaped steel plate. The peak displacements of the girder and rail were reduced by 48.1% and 47.7%, respectively. The peak deformation was reduced by 70.4%, 70.8%, and 86.1% for the fasteners, CA mortar layer and sliding layer, respectively. All of the fixed bearing were reduced to below slight damage, but the pier damage was amplified. The side piers are slightly damaged, and the drift ratio of pier top for the middle pier is 0.395%, which is just above the moderate damage limit (0.34%) and far from the severe damage limit (0.95%). Therefore, the damage to the piers is not significant, and only a small amount of repair is needed. X-EDSD can effectively enhance the seismic performance of the overall structure of the HSRTBS.

4) This study proposed a comprehensive consideration of the SRC-ECR coefficient (R_{pe}) for evaluating the effect of X-EDSD on the seismic performance of HSRTBS. The greater the thickness of the X-shaped steel plate is, the R_{pe} value decreases and then increases. It indicates that a minimum value of R_{pe} exists in the middle, which corresponds to the optimal thickness of the X-shaped steel plate. On the basis of the third-degree polynomial fitted to the curve equation, the final optimum thickness is 14.94 mm, and the Proposed engineering value is 15 mm.

X-EDSD can effectively control the response of HSRTBSs and achieve assembly and quick replacement after earthquakes. However, X-EDSD will amplify damage to piers and the arrangement is limited. Our next step is to study planar energy dissipation devices, reduce the stiffness of energy dissipation components, and balance the response of piers with other components. In addition, planar energy dissipation devices can be arranged more flexibly. Moreover, we will do the study for the modes that are perturbed and interacted in different ways by X-EDSD. Because the X-EDSD may cause some notable cross-mode behaviors.

Acknowledgements This research was financially supported by the National Key Research and Development Program of China (No. 2022YFC3004304), the National Natural Science Foundation of China (Grant No. 52378209), the Hunan Province Science and Technology Project Huxiang Young Talents Program (No. 2023RC3057), and the Xiaohe Sci-Tech Talents Special Funding under Hunan Provincial Sci-Tech Talents Sponsorship Program (No. 2023TJ-X66).

Competing interests The authors declare that they have no competing interests.

References

1. Gou H, Ran Z, Yang L, Bao Y, Pu Q. Mapping vertical bridge deformations to track geometry for high-speed railway. Steel and Composite Structures, 2019, 32(4): 467–478
2. Parsons T, Ji C, Kirby E. Stress changes from the 2008 Wenchuan earthquake and increased hazard in the Sichuan basin. Nature, 2008, 454(7203): 509–510
3. Porritt R W, Yoshioka S. Slab pileup in the mantle transition zone and the 30 May 2015 Chichi−Jima earthquake. Geophysical Research Letters, 2016, 43(10): 4905–4912
4. Shan B, Zheng Y, Liu C L, Xie Z J, Kong J. Coseismic Coulomb failure stress changes caused by the 2017 M7.0 Jiuzhaigou earthquake, and its relationship with the 2008 Wenchuan earthquake. Science China (Earth Sciences), 2017, 60(12): 2181–2189
5. Wang J, Ding L, He J, Cai F, Wang C, Zhang Z. Research of seismogenic structures of the 2016 and 2022 Menyuan earthquakes, in the Northeastern Tibetan Plateau. Remote Sensing, 2023, 15(3): 742
6. Kang X, Jiang L, Bai Y, Caprani C C. Seismic damage evaluation

of high-speed railway bridge components under different intensities of earthquake excitations. Engineering Structures, 2017, 152: 116–128
7. Li J, Zhou Y, He Z, Zhong G, Zhang C. Hysteretic behavior of cambered surface steel tube damper: Theoretical and experimental research. Frontiers of Structural and Civil Engineering, 2023, 17(4): 606–624
8. Li H, Li L, Hu R, Ye M. Simplified design of nonlinear damper parameters and seismic responses for long-span cable-stayed bridges with nonlinear viscous dampers. Frontiers of Structural and Civil Engineering, 2024, 18(7): 1103–1116
9. Wei B, Min H, Wu S, Zhong H, Jiang L, Li S, Hu Z. Investigation of equal strength mild steel tenons as displacement restraining devices for long-span railway arch bridges. Engineering Structures, 2022, 266: 114522
10. Karvanchi Y, Shekastehband B. Seismic resistance of buckling restrained steel slit panels with X-Shaped restrainers. Structures, 2023, 54: 785–807
11. Liu Z, Wang M, Hogan L S. Evaluation of seismic performance of precast concrete walls with X-shaped steel plate bracings. Structures, 2023, 48: 1548–1566
12. Cao Z, Wang Z, Du P, Liu H, Fan F. Quasi-static experiments on steel plate shear walls reinforced with X-shaped restrainers. Journal of Building Engineering, 2020, 31: 101451
13. Ding Y, Zhao C. Cyclic tests for assembled X-shaped buckling restrained brace using two unconnected steel plate braces. Journal of Constructional Steel Research, 2021, 182(4): 106680
14. Jiang L, Yu K, Jiang L, Wen T, Hu Y, Pang L. Effects of shear panel dampers on seismic response mitigation of high-speed railway simply supported bridge-track system under far-field and near-field ground motions. Archives of Civil and Mechanical Engineering, 2023, 23(2): 93
15. Jiang L, Yan Y, Wen T, Jiang L, Yu K, Pang L. System-level seismic fragility of high-speed railway track-bridge system with component-replaceable U-shaped combined steel damper. Structures. 2023, 58: 105452
16. Guo W, Chen X, Yu Y, Bu D, Li S, Fang W, Wang X, Zeng C, Wang Y. Development and seismic performance of bolted steel dampers with X-shaped pipe halves. Engineering Structures, 2021, 239: 112327
17. Naeem A, Kim J. Seismic performance evaluation of a multi-slit damper. Engineering Structures, 2019, 189: 332–346
18. Thongchom C, Ghamari A, Jaya R P, Benjeddoud O. Experimental and numerical study on an innovative trapezoidal-shaped damper to improve the behavior of CBF braces. Buildings, 2023, 13(1): 140
19. Chen Y, Ye D, Zhang L. Analytical development and experimental investigation of the casting multi-plate damper (CMPD). Engineering Structures, 2022, 250: 113402
20. Koo S, Han J, Marimuthu K P, Lee H. Determination of Chaboche combined hardening parameters with dual backstress for ratcheting evaluation of AISI 52100 bearing steel. International Journal of Fatigue, 2019, 122: 152–163
21. Wang W, Song J, Su S, Cai H, Zhang R. Experimental and numerical studies of an axial tension-compression corrugated steel plate damper. Thin-walled Structures, 2021, 163: 107498
22. Filippou F C, Popov E P, Bertero V V. Effects of bond deterioration on hysteretic behavior of reinforced concrete joints. UCB/EERC 83-19. 1983
23. Jiang L, Yu J, Zhou W, Yan W, Lai Z, Feng Y. Applicability analysis of high-speed railway system under the action of near-fault ground motion. Soil dynamics and earthquake engineering, 2020, 139: 106289
24. Yu J, Jiang L, Zhou W, Lai Z, Zuo Y, Peng K. Component damage and failure sequence of track-bridge system for high-speed railway under seismic action. Journal of Earthquake Engineering, 2023, 27(3): 656–678
25. Zhu Z, Gong W, Wang L, Li Q, Bai Y, Yu Z, Harik I E. An efficient multi-time-step method for train-track-bridge interaction. Computers & Structures, 2018, 196: 36–48
26. Yan B, Liu S, Pu H, Dai G, Cai X. Elastic-plastic seismic response of CRTS II slab ballastless track system on high-speed railway bridges. Science China. Technological Sciences, 2017, 60(6): 865–871
27. Dai G, Tang Y, Liang J, Yang L, Chen Y. Temperature monitoring of high-speed railway bridges in mountainous areas. Structural Engineering International, 2018, 28(3): 288–295
28. Jiang L, Zhang Y, Feng Y, Zhou W, Tan Z. Simplified calculation modeling method of multi-span bridges on high-speed railways under earthquake condition. Bulletin of Earthquake Engineering, 2020, 18(5): 2303–2328
29. Zhu Z, Gong W, Wang L, Bai Y, Yu Z, Zhang L. Efficient assessment of 3D train-track-bridge interaction combining multi-time-step method and moving track technique. Engineering Structures, 2019, 183: 290–302
30. Wang L, Zhu Z, Bai Y, Li Q, Costa P A, Yu Z. A fast random method for three-dimensional analysis of train-track-soil dynamic interaction. Soil Dynamics and Earthquake Engineering, 2018, 115: 252–262
31. Yu J, Jiang L, Zhou W, Liu X, Nie L, Zhang Y, Feng Y, Cao S. Running test on high-speed railway track-simply supported girder bridge systems under seismic action. Bulletin of Earthquake Engineering, 2021, 19(9): 3779–3802
32. Hu Y, Guo W. Seismic response of high-speed railway bridge-track system considering unequal-height pier configurations. Soil Dynamics and Earthquake Engineering, 2020, 137: 106250
33. Wen T, Jiang L, Jiang L, Zhou W, Du Y. Interlayer area damage modeling and damage-based seismic fragility analysis of high-speed railway bridge and track system. Engineering Structures, 2022, 272: 114989
34. Jiang L , Liu X , Yan Y , L Jiang. U-shape energy-dissipation device for enhancing seismic resilience of high-speed railway track-bridge systems. Journal of Constructional Steel Research, 2025, 226: 109257
35. Chen X, de Domenico D, LI C. Seismic resilient design of rocking tall bridge piers using inerter-based systems. Engineering Structures, 2023, 281: 115819
36. Chen X Jr, Spencer B F Jr, Li J, Guan Z, Pang Y. Optimization of distribution patterns of link beams in a double-column tall pier bent subjected to earthquake excitations. Earthquake Engineering & Structural Dynamics, 2023, 52(3): 641–659
37. Kent D, Park R. Inelastic behaviour of reinforced concrete

members with cyclic loading. Bulletin of the New Zealand Society for Earthquake Engineering, 1971, 4(1): 108–125

38. Lai Z, Jiang L. Analytical evaluation of lateral rail unevenness on high-speed railway bridge after transversal seismic shaking. Engineering Structures, 2022, 267: 114614
39. Shao G, Jiang L, Chouw N. Experimental investigations of the seismic performance of bridge piers with rounded rectangular cross-sections. Earthquakes and Structures, 2014, 7(4): 463–484
40. GB 50111-2006. Code for Seismic Design of Railway Engineering of China. Beijing: Standardization Administration of the People's Republic of China, 2006
41. Yu J, Jiang L, Zhou W, Lu J, Zhong T, Peng K. Study on the influence of trains on the seismic response of high-speed railway structure under lateral uncertain earthquakes. Bulletin of Earthquake Engineering, 2021, 19(7): 2971–2992
42. Wei B, Yang T, Jiang L, He X. Effects of friction-based fixed bearings on the seismic vulnerability of a high-speed railway continuous bridge. Advances in Structural Engineering, 2018, 21(5): 643–657
43. Wei B, Yang T, Jiang L, He X. Effects of uncertain characteristic periods of ground motions on seismic vulnerabilities of a continuous track-bridge system of high-speed railway. Bulletin of Earthquake Engineering, 2018, 16(9): 3739–3769
44. Wang Z, Jiang L, Jiang L, Zhou W, Du Y. Seismic response of high-speed railway simple-supported girder track-bridge system considering spatial effect at near-fault region. Soil Dynamics and Earthquake Engineering, 2022, 158: 107283
45. Hwang CL, Yoon KP. Multiple Attribute Decision Making Methods and Applications A State-of-the-art Survey. Berlin: Springer, 1981
46. Wen T, Jiang L, Jiang L, Jin Z, Du Y, Pang L. Repair cost assessment of longitudinal continuous ballastless track structure on high-speed railway bridge with spatially distributed interlayer area damage. Structures, 2023, 57: 105157